Effects of Microstructure on CVN Impact Toughness in Thermomechanically Processed High Strength Microalloyed Steel

TAO JIA, YANLEI ZHOU, XIAOXIAO JIA, and ZHAODONG WANG

Investigation on the correlation between microstructure and CVN impact toughness is of practical importance for the microstructure design of high strength microalloyed steels. In this work, three steels with characteristic microstructures were produced by cooling path control, *i.e.*, steel A with granular bainite (GB), steel B with polygonal ferrite (PF) and martensite-austenite (M-A) constituent, and steel C with the mixture of bainitic ferrite (BF), acicular ferrite (AF), and M-A constituent. Under the same alloy composition and controlled rolling, similar ductile-to-brittle transition temperatures were obtained for the three steels. Steel A achieved the highest upper shelf energy (USE), while large variation of impact absorbed energy has been observed in the ductile-to-brittle transition region. With apparently large-sized PF and M-A constituent, steel B shows the lowest USE and delamination phenomenon in the ductile-to-brittle transition region. Steel C exhibits an extended upper shelf region, intermediate USE, and the fastest decrease of impact absorbed energy in the ductile-to-brittle transition region. The detailed CVN impact behavior is studied and then linked to the microstructural features.

I. INTRODUCTION

TOUGHNESS, generally interpreted as the resistance to fracture, is considered as one of the most important mechanical properties for steel plate. It can be evaluated by drop weight tear test (DWTT), crack tip opening displacement (CTOD) test, or the more ordinary Charpy V-notch (CVN) impact test. Depending on the application scenario, the requirement for toughness varies. Taking the linepipe steel for example, besides the DWTT property, the requirement for the CVN impact absorbed energy at 273 K (0 °C) which normally approaches the upper shelf energy (USE) increases with the increasing strength level. And the demand for low-temperature toughness is substantially increased when the oil exploration goes to the deep sea or abyssal region. Therefore, understanding the correlation between microstructures and toughness would be crucial for the microstructure design of high strength microalloyed steel plate.

A large number of researches have been devoted to this field. Among the microstructural control measures, refining the grain size is of primary importance, since it enhances the yield strength and lowers the ductile-to-brittle transition temperatures (DBTT) at the same time. Song *et al.*[1] investigated the CVN impact behavior of an ultrafine grained C-Mn steel with "ferrite + dispersed cementite" microstructure. Compared with the initial "ferrite + pearlite" microstructure, the lower-shelf energy (LSE) was significantly raised, and the DBTT was lowered by the joint contribution of the decrease in ferrite grain size from 6.8 to 1.3 μm and the occurrence of delamination crack. Calcagnotto *et al.*[2] has produced "ferrite + martensite" dual-phase steels with different grain size by large strain warm rolling and intercritical annealing. The grain refinement was found to promote the ductile fracture mechanism, lower the DBTT, and increase the USE and LSE.

Martensite-austenite (M-A) constituent, which is formed during austenite to bainite transformation, affects the impact toughness mainly by its size. As done by Lan *et al.*,[3] the fracture stress of the M-A constituent can be calculated using the classical Griffith theory. The increase of M-A constituent size would decrease its fracture stress, and therefore increase the probability of cleavage fracture nucleated inside the M-A constituent or at the interface with the ductile matrix. The critical size that is able to suppress the cleavage fracture for different microstructures at room temperature was proposed, which is about 10 μm by Chatterjee and Bhadeshia[4] and 4 to 6 μm by Caballero *et al.*[5]

Crystallography,[6–8] as another microstructural parameter, is also important in controlling impact toughness. An increase in the volume fraction of grains with $\langle 001 \rangle$ orientation parallel to rolling direction (RD) would seriously deteriorate the impact toughness, since the

TAO JIA and ZHAODONG WANG are with the State Key Lab of Rolling and Automation, Northeastern University, 3-11 Wenhua Rd., Shenyang 110819, P.R. China. Conatct e-mail: tao.jia.81@gmail.com YANLEI ZHOU is with the Institute of Metal Research, Chinese Academy of Sciences, 72 Wenhua Rd., Shenyang 110016, P.R. China. XIAOXIAO JIA is with the Advanced Engineering Materials, the University of Manchester, Oxford Rd., Manchester M139PL, U.K.
Manuscript submitted July 29, 2016.
Article published online December 20, 2016.

{100} planes are most beneficial for cleavage fracture. In contrast, higher fraction of grains with ⟨110⟩ orientation parallel to RD would be favorable for the promotion of impact toughness because {110} slip planes are the main source of plastic deformation.

Much more efforts have been made to the study of correlation between toughness and microstructural constituent phase. Hwang et al.[9] has produced a variety of diversified microstructures using the combination of composition and cooling control. Results showed that the granular bainite (GB) was able to achieve the highest USE when compared with the lath bainite/lath martensite (LB/LM) and degenerated upper bainite (DUB). The LB/LM has resulted in the lowest DBTT, which was mainly linked with the relatively smaller grain size. In the study of Sung et al.,[10] three types of characteristic microstructures, including acicular ferrite (AF), GB, and UB, were produced by controlled rolling and cooling process in a ultra-low carbon bainitic steel. The coarse GB exhibited higher USE and DBTT when compared with UB, while the AF with the smallest effective grain size and finely distributed secondary phases had the highest USE and lowest DBTT. Kim et al.[11] has investigated the charpy impact property of API X70 linepipe steel with molybdenum and vanadium addition. Compared with rolling in "ferrite + austenite" dual-phase region, rolling in austenite single-phase region promoted the formation of AF in polygonal ferrite (PF) matrix, and therefore achieved a higher USE and lower DBTT. Using a C-Mn-Si-Cr steel and a C-Mn-B steel, Caballero et al.[5] has studied the influence of bainite morphology on room temperature impact toughness of continuously cooled cementite-free bainitic steel. When compared with lath-like UB, GB showed a lower resistance to crack propagation because of its larger crystallographic packet size and the premature crack nucleation possibly associated with the coarse M-A constituent. Except the work done by Sung et al.,[10] the above researches have one thing in common, i.e., the characteristic microstructures were all prepared by the combination of at least two variants from alloy composition, controlled rolling and cooling process. When comparison are made between two independent studies, attentions should be paid to the extra influencing factors, such as alloying element or austenite state prior to cooling which make the analysis complicated.

In recent years, the ultra-fast cooling (UFC) technology[12] has attracted wide attention. It can be used not only with lamellar cooling to realize different cooling paths, but also as an alternative to the quenching treatment. In this work, the CVN impact behavior of microstructures with different combination of constituent phases is investigated. Using a low carbon microalloyed steel, characteristic microstructures were produced by only varying the cooling path and

examined by scanning electron microscopy (SEM), transmission electron microscopy (TEM), and electron backscattered diffraction (EBSD). The impact load and absorbed energy vs displacement curves and fracture surface of the CVN impact sample are analyzed in detail to reveal the underlying connection between toughness and microstructure.

II. MATERIALS AND EXPERIMENTAL PROCEDURES

The alloy composition of the steel used is listed in Table I. It was multi-alloyed with nickel for toughness, chromium and molybdenum for hardenability, and some micro-alloying elements (niobium, titanium, and vanadium) for grain refinement and precipitation strengthening. The investigated steel was produced in laboratory by melting in a vacuum induction furnace, and then forged into slabs with a section size of 120×120 mm^2.

Using Thermo-Calc with TCFE6 database, the A_{e3} temperature (equilibrium austenite to ferrite transformation temperature) was determined to be 1098 K (825 °C). And the bainite start temperature was calculated to be 843 K (570 °C) by a computer program "mucg83.f" available from the Materials Algorithm Project website (MAP).[13]

Experimental procedure is presented in Figure 1. After homogenization at 1473 K (1200 °C) for 120 minutes, a two-step hot rolling was conducted to reduce the thickness of the slab from 120 to 12 mm. The reduction ratio for the rough and finish rolling was 49 and 69 pct, respectively. After this identical treatment for all specimens, three different cooling procedures were carried out to obtain different types of microstructures. For
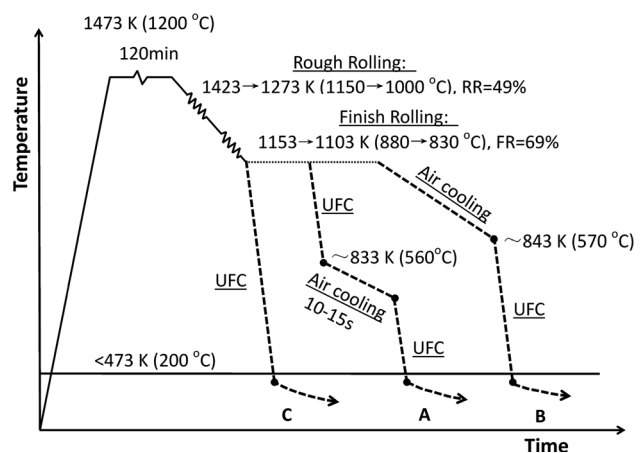

Fig. 1—Schematic illustration of the thermomechanical processing conditions for steels A, B, and C.

Table I. Alloy Composition of the Investigated Steel (wt pct)

C	Si	Mn	Cr	Ni	Cu	Mo	Nb	Ti	V	Al	P	S	N
0.07	0.27	1.62	0.23	0.4	0.26	0.23	0.065	0.017	0.034	0.04	0.004	0.0025	0.004

convenience, they are referred to as steels A, B, and C, where A, B, and C refer to the different cooling conditions. For steel A, a three-stage cooling path was employed. It was first ultra-fast cooled to around the bainite start temperature ~833 K (560 °C), followed by air-cooling (AC) for 10 to 15 seconds, and finally quenched by UFC. For steel B, a two-stage "AC + UFC" path, first AC to 843 K (570 °C) and then UFC was carried out. Steel C was directly quenched by UFC after finish rolling. In all three cases, the final temperature after the last stage UFC is below 473 K (200 °C), and the measured cooling rate of UFC and AC was above 25 K s^{-1} and about 1 K s^{-1}, respectively.

Microstructures were observed by SEM (FEI Quanta600) and TEM (FEI Tecnai G2 F20). The longitudinal-normal plane of the steel specimens was prepared with conventional metallographic techniques including grinding, polishing and etching with 4 pct Nital solution. In order to reveal the M-A constituent, Lepera reagent (1 pct $Na_2S_2O_5$ solution and 4 pct picric acid alcohol solution 1:1 blended) was used to etch the polished sample. For TEM samples, square slices with a thickness of 400 μm were cut with the wire cut electrical discharge machining and then mechanically grinded to below 50 μm with 600 to 1500 grit SiC papers. Then, Φ3 mm disks were punched and twin-jet electro-polished in a mixture of 9 pct perchloric acid and 91 pct absolute ethyl alcohol at 233 K (−40 °C) and the potential of 30 V. For EBSD analysis (resolution 0.1 μm), the SEM samples were again grinded with 1500 grit SiC papers and then electro-polished in a solution consisting of 12.5 pct perchloric acid and 87.5 pct absolute ethyl alcohol at room temperature and a potential of 20 V for 20 seconds. The total scanned area was 40×40 μm^2. The scan step size was 0.1 μm and a minimum grain size of 0.4 μm has been defined.

Standard cylindrical tensile test specimens with a gage diameter of 6 mm and a parallel gage length of 40 mm were tested at room temperature with a crosshead speed of 3 mm min^{-1} using an Instron tensile testing machine. Charpy V-notch (CVN) impact tests were conducted on an Instron Dynatup 9200 series instrumented drop weight impact tester equipped with an oscilloscope, using standard samples with a size of $10 \times 10 \times 55$ mm^3. The tests were carried out in a temperature range of 77 K to 293 K (−196 °C to 20 °C). In order to investigate the cleavage fracture behavior, the fracture surface of samples tested at 153 K (−120 °C) was afterwards observed by SEM. Both the tensile and CVN impact samples were cut along longitudinal direction, and each datum reported in this work is an average of three tests.

III. EXPERIMENTAL RESULTS

A. *Microstructure*

Figure 2 shows the SEM micrographs for steels A, B, and C. The GB, consisting of bainitic ferrite (BF) with dispersed M-A constituent inside, is the predominant constituent phase in steel A (Figure 2(a)). The middle-stage air-cooling process has promoted the formation of GB. In steel B (Figure 2(b)), the first-stage air-cooling enabled the formation of coarse PF, and the subsequent UFC promoted the transformation from carbon-enriched austenite to M-A constituent, so a typical "PF + M-A constituent" dual-phase microstructure was obtained. As for steel C (Figure 2(c)), which was directly quenched after finish rolling, a mixed microstructure that comprises BF, M-A constituent, and AF was obtained. Using Lepera reagent, the area fractions and mean size of M-A in steels A, B, and C were measured to be 28.2 ± 3.54 pct and 1.14 μm, 28.0 ± 1.17 pct and 2.24 μm, 30.4 ± 2.30 pct and 1.17 μm, respectively.

Characteristic microstructural features are presented in details in TEM images (in Figure 3), for instance, the equiaxed BF surrounding the M-A constituent in GB in steel A (Figure 3(a)), the large M-A constituent with alternating martensite and retained austenite morphology in steel B (Figure 3(b)), and the parallel lath BF (Figure 3(c)) and interlocking AF (Figure 3(d)) in steel C. Besides, the lath BF and AF in steel C have apparently larger dislocation density than equiaxed BF in steel A and PF in steel B.

Figure 4 shows the band contrast and misorientation maps obtained from EBSD analysis. Grain boundaries are displayed in different colors, where red and blue lines represent low-angle grain boundary (LAGB) and high-angle grain boundary (HAGB), respectively. In steel A (Figure 4(a)), relatively larger fraction of LAGBs are present, which separate the equiaxed BF in GBs. The M-A constituent in steel B has been subdivided into small grains by HAGBs, as shown in the magnification in Figure 4(b). In steel C (Figure 4(c)), BF presents both lath and equiaxed morphology. The chaotic spatial orientation and fine-grained interlocking morphology of AF is more clearly revealed. Some extremely small (~0.5 μm) ferrite grains, indicated by white arrow, are found in both steel A and C. When the temperature of finish rolling approached to A_{e3} temperature, the formation of ferrite was promoted by strain-induced transformation mechanism, while the grain growth was suppressed by subsequent UFC.

Figure 5 presents the distribution of grain boundary misorientation. The fraction of HAGB reaches 36.9 pct in Steel B, while that number decreases to 23.8 pct for steel A and 22.3 pct for steel C. The qualitative differentiation regarding the constituent phases and substructure are clearly reflected. Compared with the diffusional transformed ferrite phase in steel B, the bainitic phase in steel A and C exhibits characteristic distribution, *i.e.*, relatively high density of low-angle boundaries and lack of misorientation at intermediate misorientation angles.

B. *Tensile Properties*

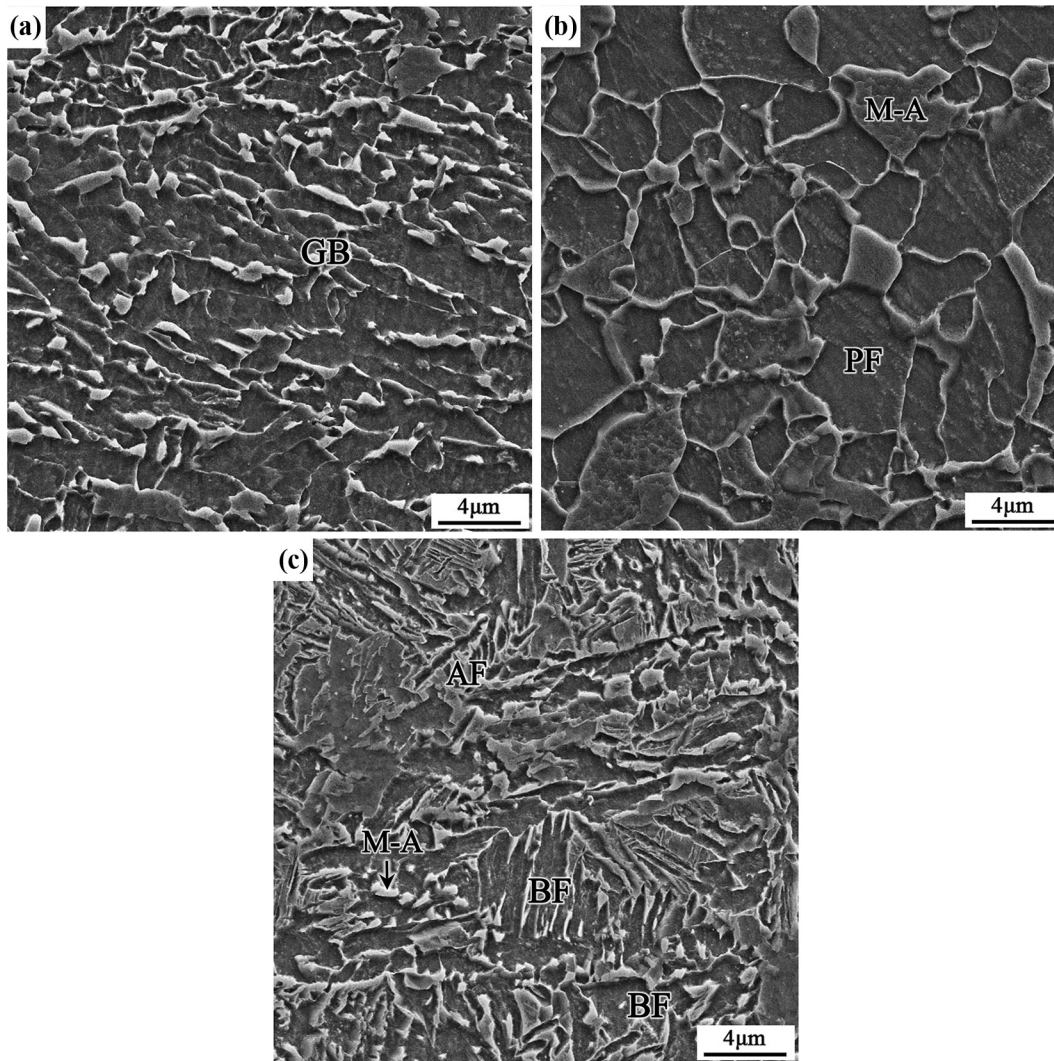Room temperature tensile test results of steels A, B, and C are listed in Table II. Steel B exhibits typical

Fig. 2—SEM micrographs of steels (a) A, (b) B, and (c) C.

tensile properties of dual-phase microstructure, *i.e.*, low yield strength (σ_y), yield ratio (YR), and high elongation (δ). Presumably because of the directly quenched microstructures (BF and AF), steel C shows the highest σ_y and ultimate tensile strength (σ_b) and thus the lowest δ. While steel A, mainly consisting of GB, has the moderate σ_y and δ, and the lowest σ_b.

Generally, yielding in multiphase steels primarily occurs in the relatively ductile phase, for steels A, B, and C, which is equiaxed BF, PF, and BF/AF, respectively. Considering the dislocation density and crystallographic size (Figures 3, 4), the σ_y would increase in the order of steel B, A, and C, which is in accord with the results in Table II. The YR, defined as the ratio of σ_y to σ_b, can be closely linked to the strain hardenability of the ductile phase during tensile test. Compared with equiaxed BF and BF/AF, the PF exhibits superior strain hardenability and thus leads to the lowest YR of steel B.

C. *CVN Impact Properties*

Figure 6 shows the CVN impact absorbed energy plotted as a function of test temperature, which is fitted with the hyperbolic tangent equation to assist the data interpretation. The DBTT, which corresponds to the average value of USE and LSE, is determined and listed in Table II. All the three steels exhibit brittle fracture behavior at the lowest test temperature that is 77 K (−196 °C). Steel A (Figure 6(a)) has the highest USE, approaching 300 J. And in the ductile-to-brittle transition region, dramatic scattering in impact absorbed energy can be observed from tests at 193 K and 153 K (−80 °C and −120 °C). While for steel B (Figure 6(b)), the slowest transition from ductile-to-brittle fracture is present even though it has the lowest USE. Steel C, as shown in Figure 6(c), exhibits an extended upper shelf region from 213 K to 293 K (−60 °C to 20 °C). And as the test
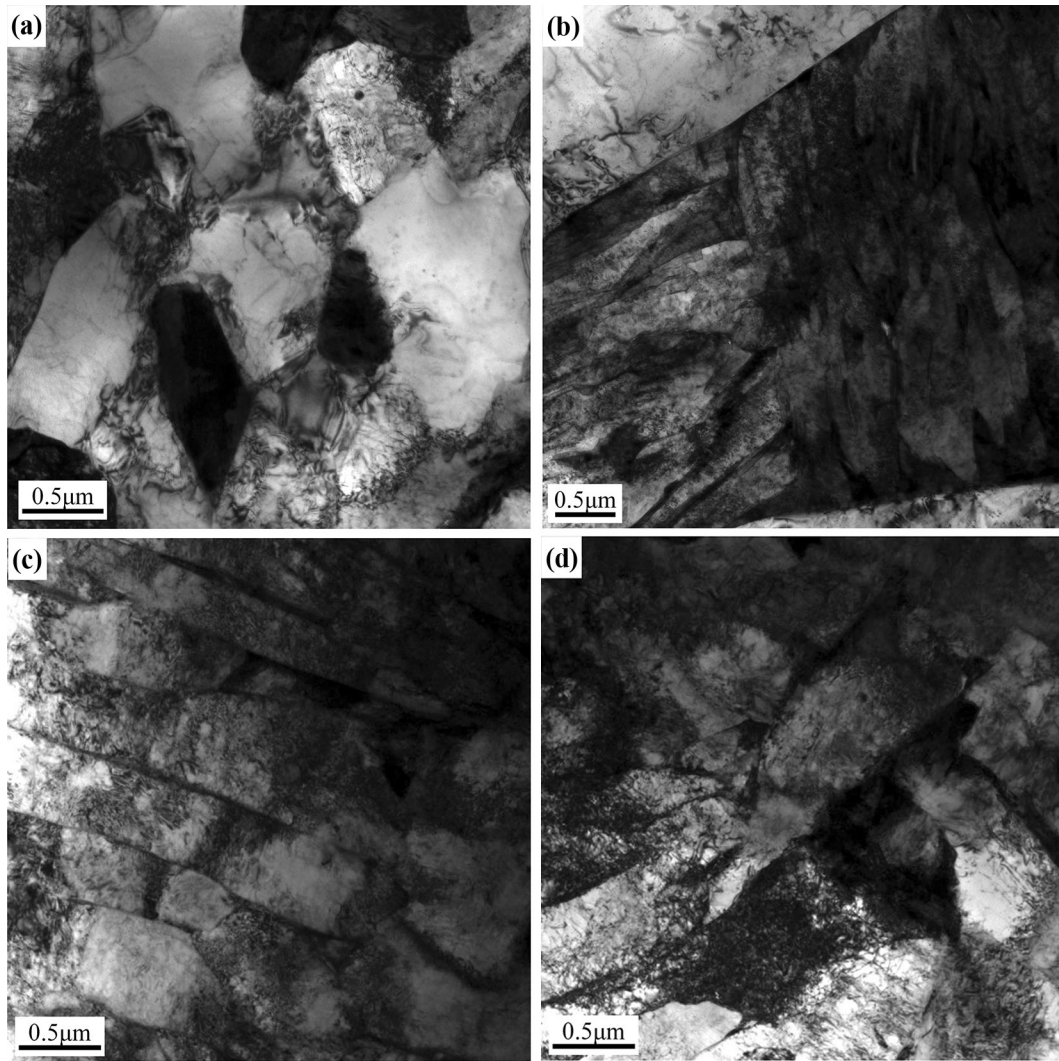
Fig. 3—TEM images showing characteristic microstructure of steels (*a*) A, (*b*) B, (*c*) and (*d*) C.

temperature decreases, the impact absorbed energy of steel C falls at a comparatively higher rate than that of steels A and B. Regardless of the significant difference in Charpy impact behaviors in upper shelf and transition regions, steels A, B, and C display comparable DBTTs, which vary between 168 K and 165 K (−105 °C and −108 °C), all showing good low-temperature toughness.

IV. DISCUSSION

A. *Ductile-to-Brittle Transition Temperature*

In the ductile-to-brittle transition region, the fracture mechanism involves a change from void coalescence to cleavage. Thus, the ductile-to-brittle transition is a result of competition between plastic flow and cleavage fracture, and is quantitatively defined as the point where the yield stress equals the cleavage fracture stress. Therefore, microstructural parameters which affect the yield stress or cleavage fracture stress would indirectly

determine the DBTT. According to Gutiérrez[14] and Isasti *et al.*[15], the DBTT obtained from CVN impact test can be related to the alloy composition and a serials of microstructural parameters:

$$
\begin{aligned}
\mathrm{DBTT} = {} & \sum_i k_{M_i}(M_i) + k_N (N_{\mathrm{free}})^{1/2} \\
& + k_1 (\mathrm{pct\ Pearlite} + \mathrm{pct\ M\text{-}A})^{1/3} + k_2 \Delta\sigma_y \\
& + k_3 D_{\mathrm{avg}}^{-1/2} + k_4 \left(D_{20\,\mathrm{pct}} / D_{\mathrm{avg}}\right)^{1/2} + k_5 D_{\mathrm{M\text{-}A}}^{1/2},
\end{aligned}
$$

[1]

where the coefficient k's are constants. (M_i) and (N_{free}) are the amount of alloying elements and free nitrogen in weight percent. Using Thermo-Calc software (TCFE6 database), the nitrogen is calculated to be consumed by forming titanium nitride and niobium carbonitride, and therefore, N_{free} is zero at room temperature. The pct pearlite is the fraction of pearlite and is zero in this work. The pct M-A and $D_{\mathrm{M\text{-}A}}$ are the fraction and
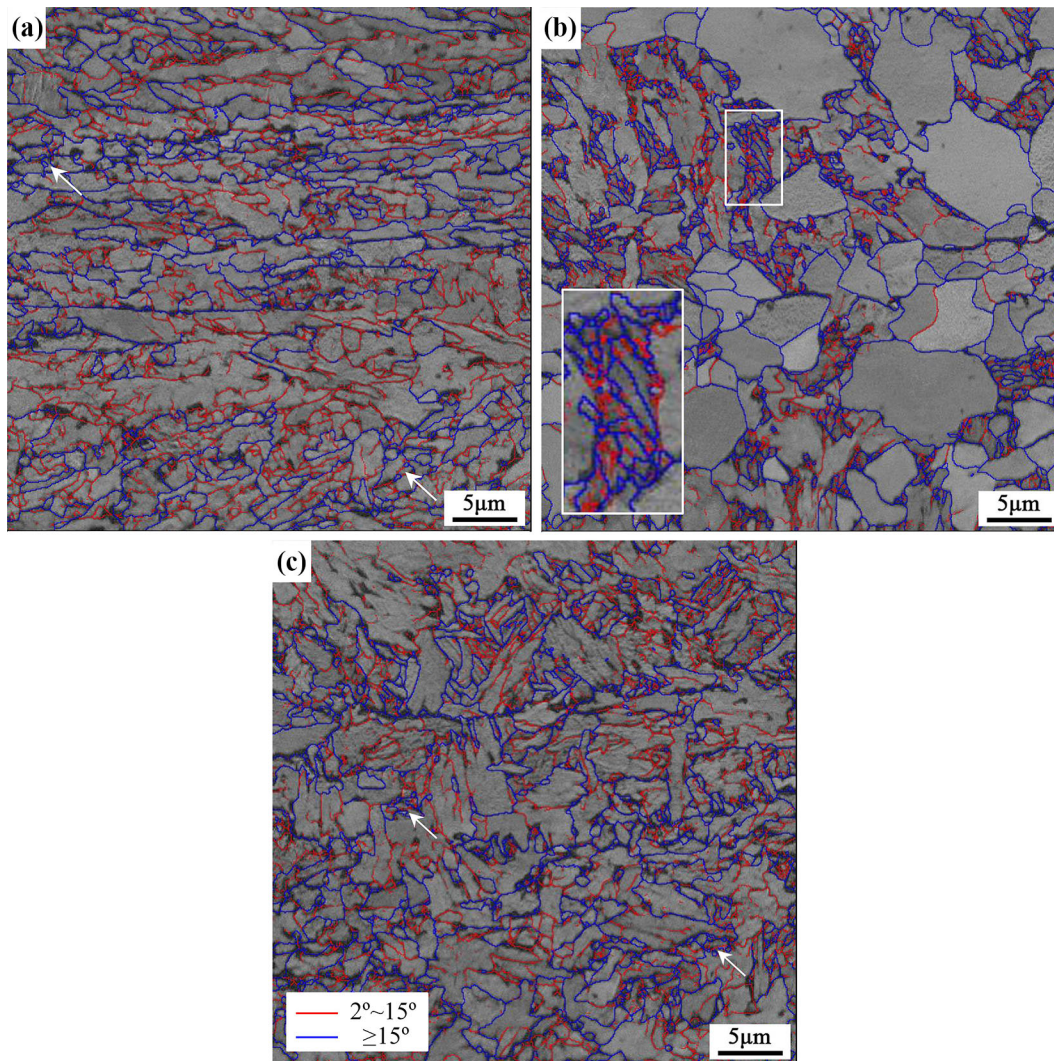
Fig. 4—EBSD band contrast map with grain boundary misorientation for steels (a) A, (b) B and (c) C.
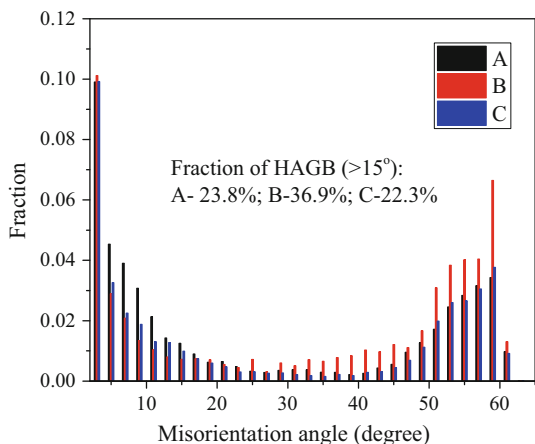

Fig. 5—Grain boundary misorientation angle distribution map.

average size of M-A constituent, respectively. $\Delta\sigma_y$ accounts for the contributed yield strength due to precipitation and dislocation. D_{avg} is the average size

of grains separated by HAGBs. The $D_{20\ pct}/D_{avg}$ describes the microstructural heterogeneity, where $D_{20\ pct}$ refers to the cutoff grain size at 80 pct area fraction in a grain size distribution histogram.

1. D_{avg} and $D_{20\ pct}$

Grain size distribution obtained from EBSD analysis is presented in Figure 7, where the grains are separated by HAGBs. As shown in Figure 7(a), steel B has the smallest D_{avg}, even though large PF grains are present. This can be explained by the fact that densely distributed HAGBs in M-A constituent provide a large fraction of HAGBs in steel B (see Figures 4(b) and 5). In steel C, owing to the small-grained AF, the amount of grains with size less than 1 μm accounts for 54 pct, which is 15 pct more grains than that in steel A (about 39 pct). All in all, the effective grain size of steels A, B, and C is calculated to be 1.95, 1.64, and 1.67 μm, respectively. Using Figure 7(b), the $D_{20\ pct}$ in steels A, B, and C is measured to be 10.63, 8.80, and 10.41 μm, respectively.

Table II. Tensile and Charpy Impact Results Presented as the Average Value of Three Specimens for Each Group

Steels	Tensile Properties				Charpy Impact Properties	
	σ_y (MPa)	σ_b (MPa)	δ (pct)	YR	USE (J)	DBTT [K (°C)]
A	568 ± 14	772 ± 33	22.8 ± 1.4	0.74	297	168 (−105)
B	509 ± 7*	823 ± 11	25.4 ± 0.6	0.62	186	166 (−107)
C	648 ± 22	880 ± 30	20.5 ± 1.0	0.74	204	165 (−108)

* 0.2 pct offset yield strength.

2. $\Delta\sigma_y$

The contributed yield strength due to precipitation and dislocation has been best demonstrated by the Pythagorean sum,[16] *i.e.*,:

$$\Delta\sigma_y = \sqrt{\Delta\sigma_{\text{Dis}}^2 + \Delta\sigma_{\text{Orowan}}^2}, \qquad [2]$$

where $\Delta\sigma_{\text{Dis}}$ and $\Delta\sigma_{\text{Orowan}}$ represent the dislocation strengthening and precipitation strengthening, respectively. Therefore, $\Delta\sigma_y$ can be estimated from the yield strength σ_y by References 17, 18:

$$\begin{aligned}
\Delta\sigma_y =& \sigma_y - (\sigma_0 + \Delta\sigma_{\text{SS}} + \Delta\sigma_{\text{GB}}) \\
=& \sigma_y - \Big[53.9 + 31.4(\text{Mn}) + 83(\text{Si}) + 39(\text{Cu}) \\
& + 11(\text{Mo}) - 31(\text{Cr}) + 17.4\big(D'_{\text{avg}}\big)^{-1/2}\Big],
\end{aligned} \qquad [3]$$

where σ_0 is the friction stress of ferritic matrix, $\Delta\sigma_{\text{SS}}$ the solid solution strengthening, and $\Delta\sigma_{\text{GB}}$ the grain boundary strengthening. D'_{avg} is the average grain size of the ductile phase. As a first approximation, it is calculated as $(D_{\text{avg}} - D_{\text{M-A}} \times \text{pct M-A})/(1 - \text{pct M-A})$ for steels A and C. While for steel B, it is determined from direct measurement of PF grain size from Figure 4(b). D'_{avg} is found to be 2.27, 2.42, and 1.90 μm for steels A, B, and C, respectively. Then $\Delta\sigma_y$ can be calculated.

The values of microstructural parameters in Eq. [1] are summarized in Table III. In order to fit Eq. [1] to the experimental data, selection of coefficients is made as follows. The k_2 and k_3 are taken from References 19 and 20, respectively. Other coefficients can be found in References 14 and 15 except k_5 which is set as a fitting parameter. The following modified equation is finally obtained for the DBTT, *i.e.*,:

$$\begin{aligned}
\text{DBTT} =& -11(\text{Mn}) + 42(\text{Si}) - 30(\text{Ni}) + 15(\text{Cu}) \\
& + 6(\text{Mo}) + 700(N_{\text{free}})^{1/2} + 15(\text{pct M-A})^{1/3} \\
& + 0.45\Delta\sigma_y - 13.7 D_{\text{avg}}^{-1/2} + 39\big(D_{20\,\text{pct}}/D_{\text{avg}}\big)^{1/2} \\
& + 46 D_{\text{M-A}}^{1/2}
\end{aligned} \qquad [4]$$

The individual contribution to DBTT is presented in Figure 8. Taking steel A as a reference, it is shown that the advantage achieved by refined D_{avg} is mainly balanced by the large $D_{\text{M-A}}$ in steel B, and by the increased $\Delta\sigma_y$ and $D_{20\,\text{pct}}/D_{\text{avg}}$ in steel C. Using the chemical composition and microstructural parameters in
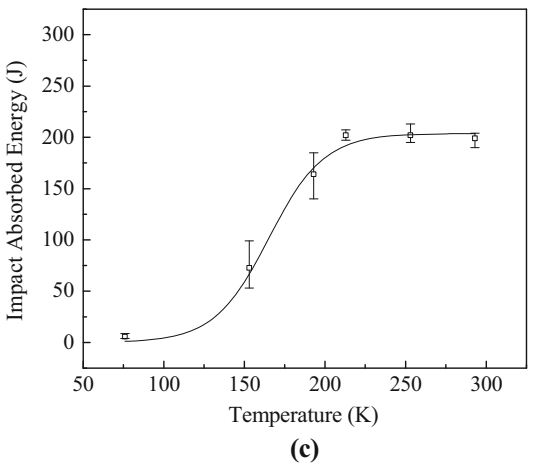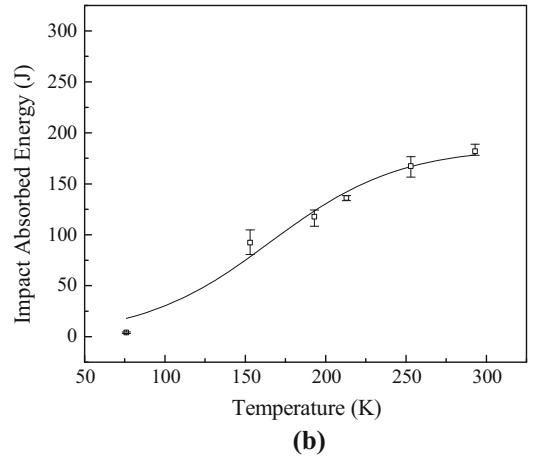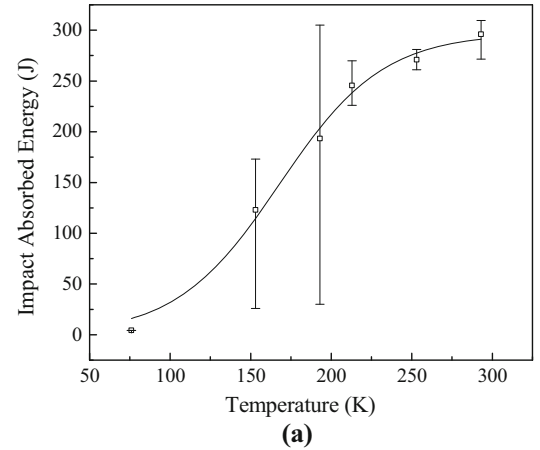

Fig. 6—CVN impact absorbed energy *vs* temperature for steels (*a*) A, (*b*) B, and (*c*) C.

(a)

(b)
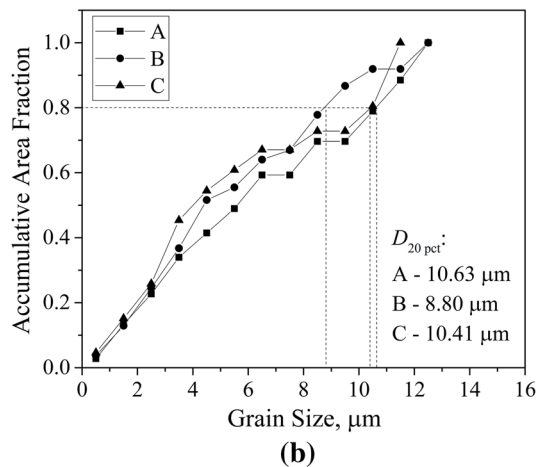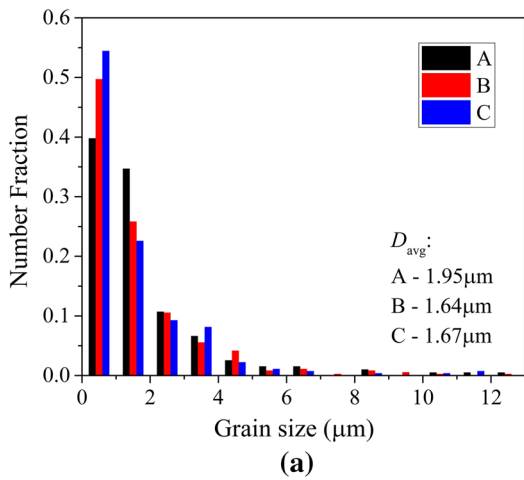
Fig. 7—Grain size distribution plotted in terms of (*a*) number fraction; (*b*) accumulated area fraction.
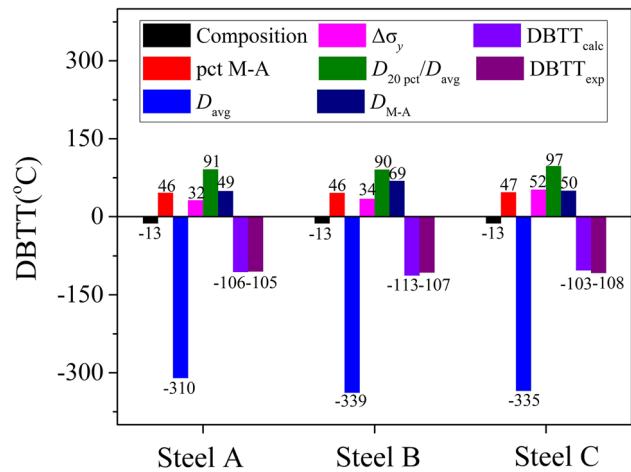

Fig. 8—Individual contribution of chemical composition and microstructural parameters to DBTT for steels A, B and C.

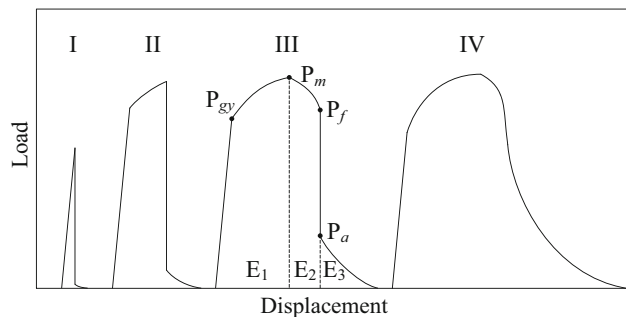Fig. 9—Schematics of four typical impact load *vs* displacement curves.

Table III. Values of the Microstructural Parameter Affecting DBTT

Steels	pct M-A	$\Delta\sigma_y$	D_{avg}	$D_{20\,pct}/D_{avg}$	D_{M-A}
A	28.2	70.0	1.95	5.45	1.14
B	28.0	75.9	1.64	5.37	2.24
C	30.4	115	1.67	6.22	1.17

Eq. [1], DBTT can be predicted with a good accuracy, *i.e.*, ±6K (±6 °C) in this work.

B. Fracture Behavior in the Upper Shelf Region

The impact fracture behavior can be investigated with the load-displacement curve generated from instrumented CVN impact test. As illustrated in Figure 9, there are in generally four types of load-displacement curves[21], that are, cleavage fracture initiated at the elastic stage (type I), after some amount of plasticity (type II), beyond the maximum load (type III), or fully ductile fracture (type IV). In the load-displacement curve, characteristic points are defined including P_{gy} the load at general yield, P_m the maximum load, P_f the load at the initiation of brittle fracture, and P_a the load at the end of brittle fracture. The fast load drop observed on the load-displacement curve of an instrumented CVN impact test can be associated with the cleavage portion of the fracture surface.[22] Then the impact absorbed energy for crack initiation stage E_1, ductile crack propagation stage E_2, and post-brittle fracture stage E_3 can be determined as indicated in type III impact load–displacement curve in Figure 9.

The difference in USE of steels A, B, and C can be studied by analyzing the impact load and absorbed energy *vs* displacement curves in Figure 10. All the three load-displacement curves display fully ductile fracture behavior, *i.e.*, type IV in Figure 9. On the load–displacement curve for steel A (Figure 10(a)), a region near the end of the test whereby the rate of load decrease is substantially reduced appeared. This feature is considered to be associated with increased loading on the striker from the specimen "wrapping around" the striking edge and/or, if the bending angle is very high, the specimen being forced through the anvils with a resultant side loading.[22]

Characteristic loads and E_i are summarized in Table IV. The P_{gy} and P_m at room temperature, in general, corresponds to the σ_y and σ_b, respectively. The USE is determined by microstructural parameters that can influence the energy absorption during ductile
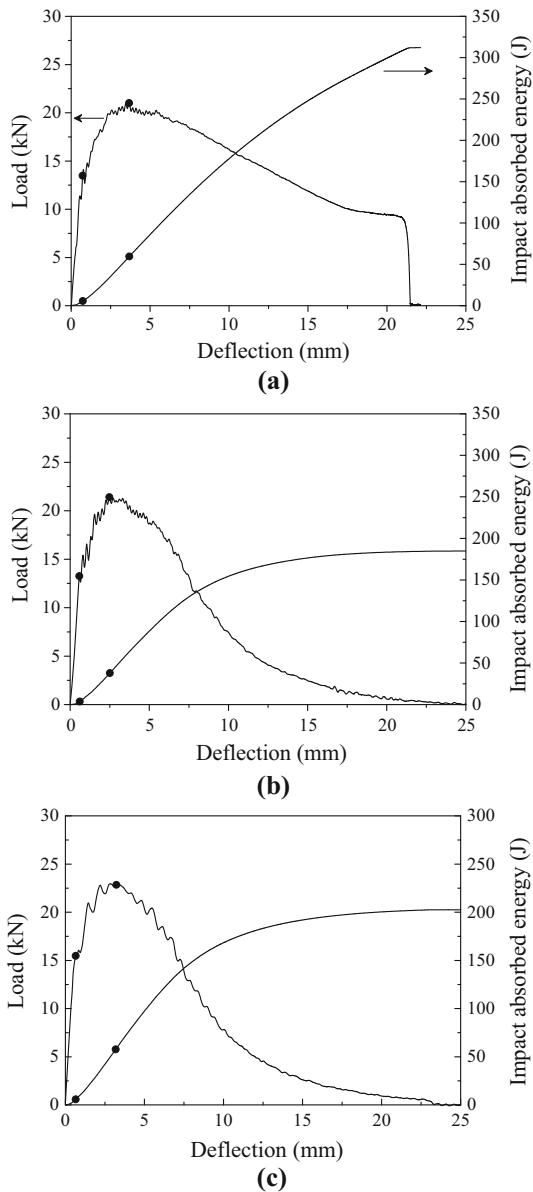

Fig. 10—The impact load and absorbed energy *vs* displacement curve at 293 K (20 °C) for steels (*a*) A, (*b*) B and (*c*) C.

fracture, which are, the nucleation, growth, and coalescence of voids.[23] For void nucleation, the most susceptible sites are the interfaces between hard second-phase particles (for example, M-A constituent) and ductile matrix. In steel B, in spite of its smallest effective grain size, the broad ferrite/M-A constituent interfaces can provide ideal sites for stress concentration, leading to the early void nucleation and the smallest E_1. By refining the M-A constituent, as is done in steels A and C, the progress of stress concentration is slowed down and the critical moment for void nucleation is delayed. Therefore, compared with steel B, both steels A and C achieved 12.2 J more for E_1. In later stage of void growth and coalescence, the crucial factors are the size of plastic zone at the crack tip and its plasticity, which are determined by the amount of mobile dislocation. Alternatively, $E_2 + E_3$ can be interpreted as the extent of difficulty for crack propagation. As presented in Figure 10, steels B and C both exhibit a smooth and relatively fast load decrease after reaching the P_m. When deflection reached 15 mm, the impact load of steels B and C both fell to below 5 kN, while it remains higher than 10 kN for steel A. It is suggested that the equiaxed BF is more effective than PF and the mixed microstructure of BF and AF in blocking the crack propagation, resulting in an extra of about 100 J for $E_2 + E_3$. By refining the grain size, GB can be a superior candidate in enhancing the USE.

C. Fracture Behavior in Ductile-to-Brittle Transition Region

Temperature effect on the fracture behavior in ductile-to-brittle transition region can be studied using steel C which exhibits typical III impact load and absorbed energy *vs* displacement curves as shown in Figure 11. The characteristic loads and E_i are summarized in Table IV. It can be found that the brittle fracture initiates at higher load and stops at lower load as test temperature decreases. The P_a/P_m, as an indication of brittle crack arrestability, also decreases with decreasing test temperature. Correspondingly, E_2 and E_3 display the same trend, while E_1 remains at the same level.

Microstructural effect on fracture behavior in the transition region is investigated by analyzing the fractured surface of the impact test sample. Figure 12 shows the SEM fractographs of steels A, B, and C tested at 153 K (−120 °C). The sample of steel A with the lowest impact absorbed energy was selected for analysis. Figures 12(a) and (b) present river-pattern fracture mode, indicating a completely cleavage fracture of steel

Table IV. Test Data from Instrumented Charpy Impact Experiments

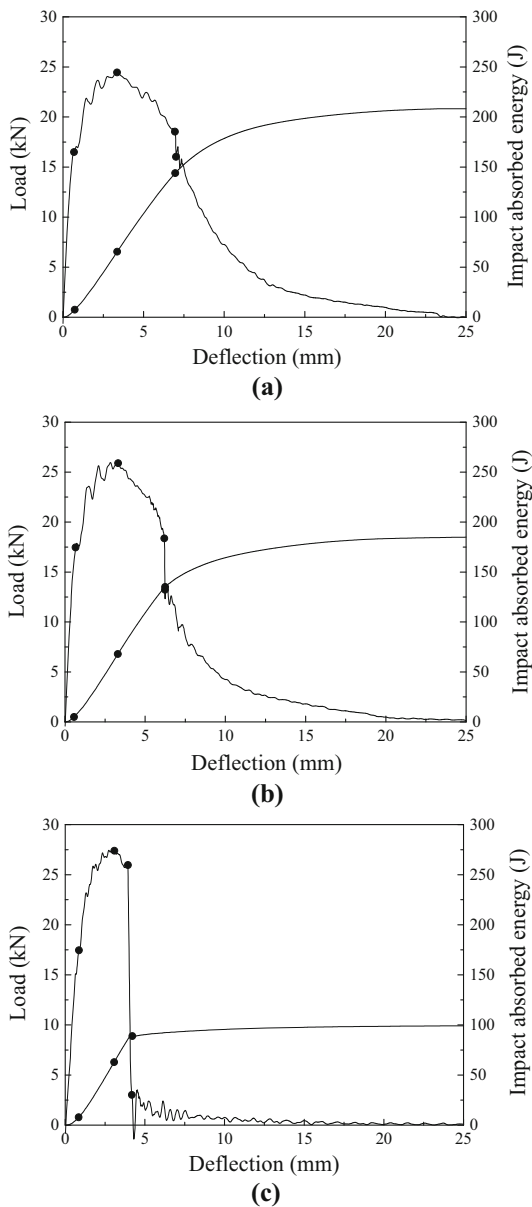| Steels	Temperature [K (°C)]	P_{gy} (kN)	P_m (kN)	P_f (kN)	P_a (kN)	P_a/P_m	E_1 (J)	E_2 (J)	E_3 (J)
A	293 (20)	13.5	21.0	—	—	—	59.5	252.6	
B	293 (20)	13.2	21.4	—	—	—	37.3	147.6	
C	293 (20)	15.5	22.9	—	—	—	59.5	143.1	
	213 (−60)	16.5	24.4	18.5	16.0	0.66	65.9	77.8	64.5
	193 (−80)	17.5	25.9	18.4	13.2	0.51	68.9	65.5	50.6
	153 (−120)	17.5	27.4	26.0	2.9	0.11	62.8	26.1	10.2

Fig. 11—The impact load and absorbed energy *vs* displacement curve for steel C at (*a*) 213 K (−60 °C); (*b*) 193 K (−80 °C); and (*c*) 153 K (−120 °C).

A. Voids can be found at the initiation site of cleavage fracture, which could possibly form by debonding of BF and M-A constituent.[24] The critical size of M-A constituent that can induce cleavage fracture can be determined according to the Griffith equation and the calculated maximum principal stress.[25] When the probability of finding the M-A constituent larger than the critical size is close to 50 pct, the crack propagation could be either ductile or cleavage.[26] This may explain the observed scattering of the impact absorbed energy in Figure 6(a). Steel C exhibits quasi-cleavage fracture with relatively small cleavage facets, indicating short cleavage fracture unit length (Figures 12(e) and (f)), this is linked to the relatively small grain size of steel C. Ductile

fracture bands (tear ridges) with small dimples were also observed in steel C. The connection of cleavage facets by tear ridges is considered as the major energy-absorbing mechanism during cleavage crack propagation.[27,28]

The fracture surface of steel B consists of smooth delamination/splits and dimpled fracture in alternating sequence (Figures 12(c) and (d)). The delamination is characteristic of the sample tested in the transition region and becomes more pronounced with decreasing testing temperature. It is proposed by Song *et al.*[1] and Arnoult *et al.*[29] that delamination leads to the decrease of DBTT. By delamination, the triaxial stress state at the crack tip is relaxed because the stress component along the thickness direction of the plate is reduced to zero. Then the global plane-strain fracture transforms into a series of local plane-stress failure, which could increase the toughness. Delamination cracks were found to be easily promoted by microstructural features like combination of soft and hard phase,[30] elongated ferrite grain shapes,[31] aligned particles and inclusions,[32] and a high intensity of {100} plane.[7,8] By analyzing the EBSD data, the fraction of grains with {100} plane parallel to the rolling plane was 5.15, 4.36, and 6.33 pct for steels A, B, and C, respectively. Therefore, in steel B, the main factor inducing the delamination cracks is dual-phase microstructure, which composed of soft PF and hard M-A constituent, rather than the intensity of {100} plane.

V. CONCLUSION

In this study, three high strength microalloyed steel plates with various microstructures were fabricated by controlling cooling path, and then their characteristic CVN impact toughness is investigated and linked to microstructural characterization.

1. The "UFC + AC + UFC" cooling path enabled the formation of microstructure with GB, while the "AC + UFC" cooling path resulted in the dual-phase microstructure of "PF + M-A constituent." A mixture of BF, AF, and M-A constituent was produced by direct UFC.
2. A modified equation predicting DBTT is proposed. Grain refinement, decreased strengthening from dislocation and precipitation, reduced fraction and size of M-A constituent, and microstructural homogeneity are favorable to achieve lower DBTT.
3. In the upper shelf region, fully ductile fracture was observed in every steel. In the two-stage cooled steel, the broad interfaces between large-sized PF and M-A constituent account for the early void formation and then the smallest E_1. The three-stage cooled steel exhibited the highest USE of 297 J, suggesting GB as a superior candidate for improving the USE.
4. In contrast to the ultra-fast cooled steel, the three-stage cooled steel showed a dramatic scattering of impact absorbed energy in the ductile-to-brittle transition region, which could be possibly related with the 50 pct possibility of either ductile or
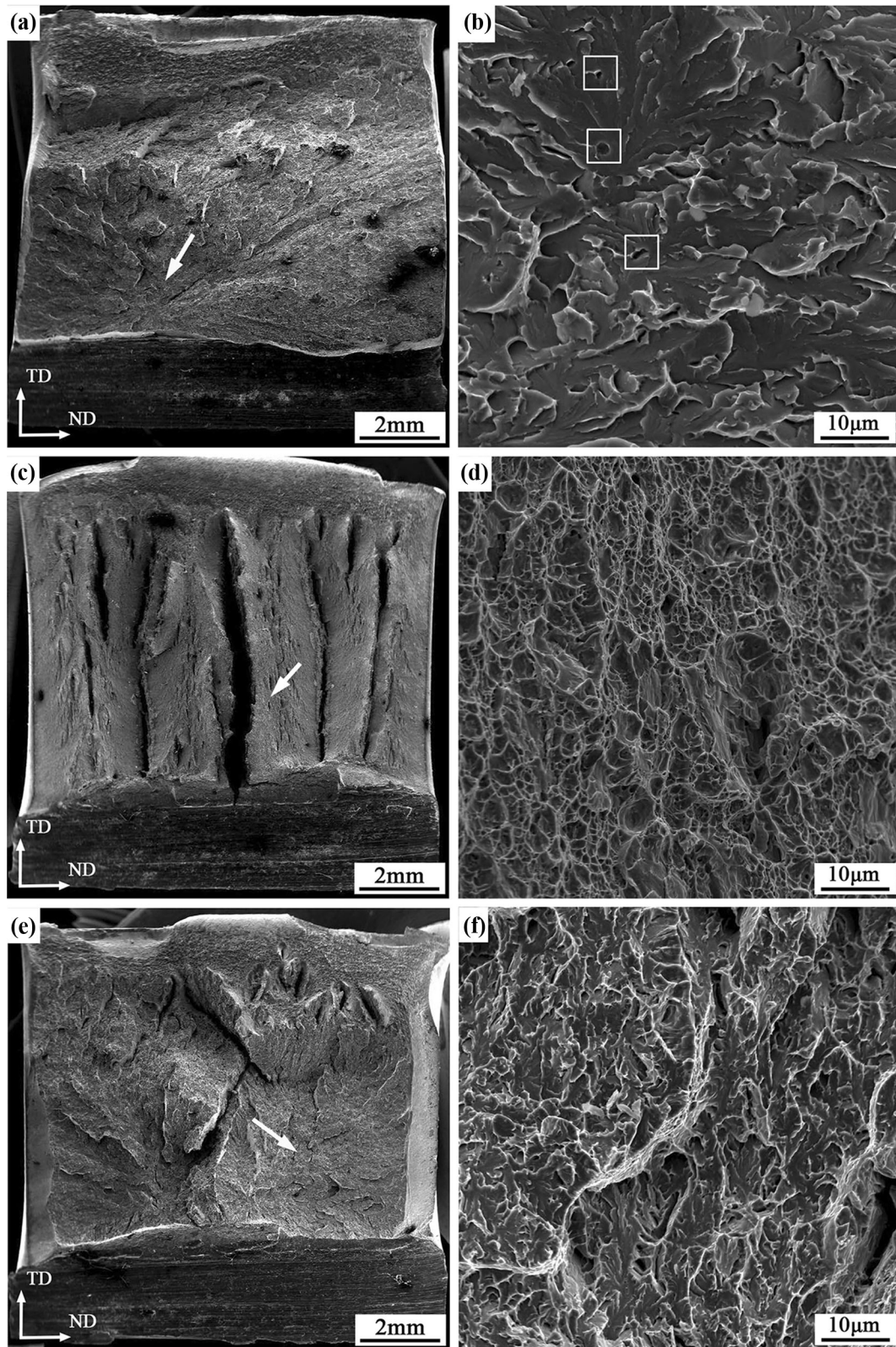
Fig. 12—SEM fractographs of steels (*a*) A, (*c*) B, and (*e*) C tested at 153 K (−120 °C), and the corresponding magnification (*b*), (*d*), and (*f*), respectively.

cleavage fracture. The two-stage cooled steel tested in this region displayed characteristic delamination crack that is able to improve the toughness and thus lower the DBTT.

REFERENCES

1. R. Song, D. Ponge, and D. Raabe: *Acta Mater*., 2005, vol. 53, pp. 4881–92.
2. M. Calcagnotto, D. Ponge, and D. Raabe: *Mater. Sci. Eng. A*, 2010, vol. 527, pp. 7832–40.
3. L.Y. Lan, C.L. Qiu, D.W. Zhao, X.H. Gao, and L.X. Du: *Mater. Sci. Eng. A*, 2011, vol. 529, pp. 192–200.
4. S. Chatterjee and H.K.D.H. Bhadeshia: *Mater. Sci. Technol*., 2006, vol. 22, pp. 645–49.
5. F.G. Caballero, H. Roelofs, C. St. Hasler, C. Capdevila, J. Cornide, and C. Garcia-Mateo: *Mater. Sci. Technol*., 2012, vol. 28 (1), pp. 95–102.
6. G.J. Baczynski, J.J. Jonas, and L.E. Collins: *Metall. Mater. Trans. A*, 1999, vol. 30A, pp. 3045–54.
7. X.L. Yang, Y.B. Xu, X.D. Tan, and D. Wu: *Mater. Sci. Eng. A*, 2014, vol. 607, pp. 53–62.
8. X.L. Yang, Y.B. Xu, X.D. Tan, and D. Wu: *Mater. Sci. Eng. A*, 2015, vol. 641, pp. 96–106.
9. B. Hwang, C.G. Lee, and T. Lee: *Metall. Mater. Trans. A*, 2010, vol. 85A, pp. 85–96.
10. H.K. Sung, S.Y. Shin, B. Hwang, C.G. Lee, N.J. Kim, and S. Lee: *Metall. Mater. Trans. A*, 2011, vol. 42A, pp. 1827–35.
11. Y.M. Kim, S.Y. Shin, H. Lee, B. Hwang, S. Lee, and N.J. Kim: *Metall. Mater. Trans. A*, 2007, vol. 38A, pp. 1731–42.
12. B.X. Wang, Z.D. Wang and G.D. Wang: *Proc. Iron Steel Technol*., Association for Iron and Steel Technology, Indianapolis. 2014, vol. 3. pp. 3073–80.
13. Materials Algorithms Project (MAP) University of Cambridge, Cambridge. 2015. http://www.msm.cam.ac.uk/map/.
14. I. Gutiérrez: *Mater. Sci. Eng. A*, 2013, vol. 571, pp. 57–67.
15. N. Isasti, D. Jorge-Badiola, M. Taheri, and P. Uranga: *Metall. Mater. Trans. A*, 2014, vol. 45A, pp. 4972–82.
16. A.J.E. Foreman and M.J. Makin: *Can. J. Phys*., 1967, vol. 45, pp. 511–17.
17. F.B. Pickering: *Physical Metallurgy and the Design of Steels*, Applied Science Publisher, London, 1978.
18. J.F. Lu, O. Omotoso, J.B. Wiskel, D.G. Ivey, and H. Henein: *Metall. Mater. Trans. A*, 2012, vol. 43A, pp. 3043–61.
19. B. Mintz, W.B. Morrison, and A. Jones: *Met. Technol*., 1979, vol. 6, pp. 252–60.
20. K.J. Irvine, F.B. Pickering, and T. Gladman: *J. Iron Steel Inst*., 1967, vol. 205, p. 161.
21. G. Puppala, A. Moitra, S. Sathyanarayanan, R. Kaul, G. Sasikala, R.C. Prasad, and L.M. Kukreja: *Mater. Des*., 2014, vol. 59, pp. 509–15.
22. R.K. Nanstad, M.A. Sokolov: *Symposium on Pendulum Impact Machine: Procedures and Specimens for Verification*, Montreal, 1994, Report No. CONF-9405223-2.
23. I.A. Yakubtsov, P. Poruks, and J.D. Boyd: *Mater. Sci. Eng. A*, 2008, vol. 480, pp. 109–16.
24. Y.L. Zhou, T. Jia, X.J. Zhang, Z.Y. Liu, and R.D.K. Misra: *Mater. Sci. Eng. A*, 2015, vol. 626, pp. 352–61.
25. S. Lee, S. Kim, B. Hwang, B.S. Lee, and C.G. Lee: *Acta Mater*., 2002, vol. 50, pp. 4755–62.
26. K. Shi, H. Hou, J.B. Chen, L.T. Kong, H.Q. Zhang, and J.F. Li: *Steel Res. Int*., 2016, vol. 87, pp. 165–72.
27. Y.L. Zhou, T. Jia, X.J. Zhang, Z.Y. Liu, and R.D.K. Misra: *J Mater. Process. Technol*., 2015, vol. 219, pp. 314–20.
28. P. Haušild, I. Nedbal, C. Berdin, and C. Prioul: *Mater. Sci. Eng. A*, 2002, vol. 335, pp. 164–74.
29. X.C. Arnoult, M. Růžičková, and K. Kunzová: *Frattura ed Integrità Strutturale*, 2016, vol. 35, pp. 509–22.
30. M.S. Joo, D.W. Suh, J.H. Bae, and H.K.D.H. Bhadeshia: *Mater. Sci. Eng. A*, 2012, vol. 546, pp. 314–22.
31. B.L. Bramfitt and A.R. Marder: *Metall. Mater. Trans. A*, 1977, vol. 8A, pp. 1263–73.
32. A.J. McEvely and R.H. Rush: *Trans. ASM*, 1962, vol. 55, pp. 654–66.